CrossMark
← click for updates

Pt$_{74}$Ag$_{26}$ nanoparticle-decorated ultrathin MoS$_2$ nanosheets as novel peroxidase mimics for highly selective colorimetric detection of H$_2$O$_2$ and glucose†

Shuangfei Cai, Qiusen Han, Cui Qi, Zheng Lian, Xinghang Jia, Rong Yang* and Chen Wang*

To extend the functionalities of two-dimensional graphene-like layered compounds as versatile materials, the modification of transition metal dichalcogenide nanosheets such as MoS$_2$ with metal nanoparticles is of great and widespread interest. However, few studies are available on the preparation of bimetallic nano-particles supported on MoS$_2$. Herein, a facile and efficient method to synthesize MoS$_2$–PtAg nanohybrids by decorating ultrathin MoS$_2$ nanosheets with octahedral Pt$_{74}$Ag$_{26}$ alloy nanoparticles has been reported. The as-prepared MoS$_2$–Pt$_{74}$Ag$_{26}$ nanohybrids were investigated as novel peroxidase mimics to catalyze the oxidation of classical peroxidase substrate 3,3′,5,5′-tetramethylbenzidine (TMB) in the presence of H$_2$O$_2$, producing a blue colored reaction and exhibiting typical Michaelis–Menten kinetics. MoS$_2$–Pt$_{74}$Ag$_{26}$ has a higher affinity for H$_2$O$_2$ than horseradish peroxidase (HRP) and a higher v_{max} value with TMB as the substrate than MoS$_2$. The improved catalytic activity of hybrids for colorimetric reactions could be attributed to the synergistic effects of octahedral Pt$_{74}$Ag$_{26}$ nanoparticles and ultrathin MoS$_2$ nanosheets as supports. Mean-while, the generation of active oxygen species ($^{\bullet}$OH) by H$_2$O$_2$ decomposition with MoS$_2$–Pt$_{74}$Ag$_{26}$ was responsible for the oxidation of TMB. On the basis of these findings, a colorimetric method based on MoS$_2$–Pt$_{74}$Ag$_{26}$ nanohybrids that is highly sensitive and selective was developed for glucose detection. Lower values of the limit of detection (LOD) were obtained, which is more sensitive than MoS$_2$ nanosheets.

1. Introduction

Since the pioneering discovery of monolayer graphene in 2004,[1] increasing attention has been paid to other two-dimen-sional (2D) layered materials, such as layered transition metal dichalcogenides (LTMDs).[2–4] One of the typical materials is mono- and few-layer molybdenum disulfide (MoS$_2$), which has received significant attention because of its tunable energy bandgap and natural richness.[5–7]

Owing to abundant active edges and a large specific surface area, graphene-like MoS$_2$ provides a promising support material for potential catalytic performance. To potentially extend the functionalities of 2D MoS$_2$ as versatile materials, modifying MoS$_2$ with 0D metal nanoparticles (NPs) to form 2D–0D multifunctional hybrid materials is of great and wide-spread interest. Many monometallic NPs, such as Au,[8] Ag,[9]

Pd,[10] Pt,[11] Ni[12] and Co[13] NPs have been successfully decorated on 2D MoS$_2$ nanosheets. These MoS$_2$–NP hybrid materials not only enhance the intrinsic properties of the materials but also bring novel properties and functions, thus providing great opportunities in developing novel optical biosensors and advanced electrocatalysts for energy conversion. So far, however, the studies on the preparation of bimetallic NPs (BNPs) supported on MoS$_2$ are extremely rare.

BNPs consist of two metals and often display enhanced catalytic performance than their monometallic counterparts because of a synergistic effect. Among them, Pt-based BNPs are presently being widely used as essential catalytic sub-stances in various fields owing to the modified geometric and electronic structures of Pt. For example, PtAg NPs have been used in methanol oxidation reactions due to their high electro-catalytic activity. Recently, many groups have started to work on MoS$_2$–BNP nanostructures. Ma's group has reported improved hydrazine oxidation activities using a NiFe alloy sup-ported on MoS$_2$ by electrodeposition and electroplating approaches.[14] In spite of effectiveness of an *in situ* growth method of BNPs on MoS$_2$, to develop a simple method for dis-persing BNPs on MoS$_2$ is highly appealing. Fan's group has

CAS Key Lab for Biological Effects of Nanomaterials and Nanosafety, National Center for Nanoscience and Technology, Beijing 100190, P. R. China.
E-mail: yangr@nanoctr.cn, wangch@nanoctr.cn

prepared MoS_2 nanosheet supported AuPd BNPs with a core–shell structure by a co-reduction method and the resulting MoS_2–AuPd exhibited excellent peroxidase-like activity.[15] Although this method is facile, the lack of a stabilizer often leads to aggregation of the products. Most recently, Wang's group employed a seeded growth strategy to achieve the controllable synthesis of Au@Pt core–shell nanodendrites on MoS_2 nanosheets, which displayed much higher electro-catalytic activity and stability than MoS_2–Pt or the commercial Pt/C catalyst.[16] Until now, the facile preparation of MoS_2–BNP hybrids with high-quality and different heterostructures still remains a challenge.

The accurate detection of H_2O_2 and glucose is of critical significance in many fields involving food, chemistry, biology, clinical control, and environmental protection.[17] Presently, colorimetric methods for H_2O_2 and glucose detection are particularly attractive for point-of-care applications because of their low cost, simplicity, and practicality.[18] In this contribution, we report a facile and efficient method to synthesize MoS_2–PtAg nanohybrids by decorating ultrathin MoS_2 nanosheets with octahedral $Pt_{74}Ag_{26}$ alloy NPs. MoS_2 nanosheets prepared by liquid exfoliation were functionalized with polyallylamine hydrochloride (PAH), and then the MoS_2–PtAg nanohybrids were obtained through a hydrothermal synthesis. This approach may represent a significant step toward the missing link between the synthesis of high-quality MoS_2–BNP nano-hybrids and their multiple promising applications, as firstly exemplified by the detection of H_2O_2 and glucose in this study.

2. Results and discussion

2.1 Preparation and characterization of MoS_2–PtAg hybrid nanomaterials

A schematic illustration of the synthesis of MoS_2–PtAg hybrid nanomaterials is illustrated in Fig. 1 and detailed in the
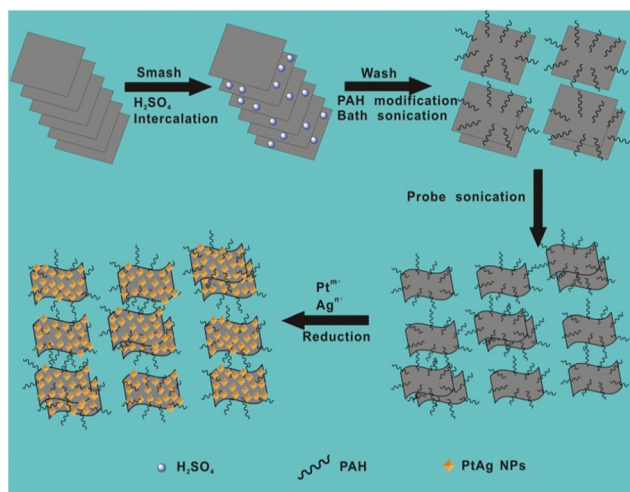

Fig. 1 Schematic illustration of synthesis of MoS_2–PtAg hybrid nanomaterials.

Experimental section. In a typical experiment, the MoS_2 nanosheets were prepared *via* a liquid exfoliation method. Briefly, commercial MoS_2 powder was first ground and then intercalated with concentrated H_2SO_4, which breaks the van der Waals interaction forces in bulk MoS_2. Subsequently, the H_2SO_4-intercalated intermediate was collected by centrifugation and repeatedly washed with ultrapure water to remove residual H_2SO_4. After that, the obtained intermediate was functionalized with a highly hydrophilic surfactant PAH through physical adsorption in water under bath sonication conditions, followed by probe sonication treatment to give MoS_2–PAH nanosheets.

Among the various known strategies for the fabrication of ultrathin MoS_2 nanosheets, the mechanical exfoliation[19] process is simple, but limited by the low yield; chemical vapour deposition (CVD)[20] yields large flake sizes but often at the cost of crystalline quality and thickness control; the chemical exfoliation[21] process gives large quantities of nanosheets but requires relatively higher reaction temperature (*e.g.* 100 °C), long duration (*e.g.* 3 days) and a lack of controllability over the degree of lithium insertion; the electrochemical exfoliation[22] process requires sophisticated instrumentation, that is, a lithium ion battery in an Ar-filled glove box connected to a battery test system. Moreover, the lithium intercalation–exfoliation process often results in a crystalline structure transformation from 2H-MoS_2 (hexagonal, semiconducting) to 1T-MoS_2 (octahedral, metallic). Specifically, the lithium intercalated compound Li_xMoS_2 is extremely sensitive to air, flammable, and the metallic Li violently reacts with H_2O to produce H_2 gas during the exfoliation process, which is dangerous. A relatively new approach is the liquid exfoliation[23] process by direct sonication in commonly used solvents involving *N*-methylpyrrolidone (NMP) and isopropyl alcohol (IPA), which was initially proposed by Coleman *et al.* in 2011. Unlike the lithium intercalation–exfoliation process, the crystalline structure of MoS_2 can be well retained by liquid exfoliation. Herein, we used a modified liquid exfoliation method to obtain MoS_2 nanosheets. Compared to the reported routes for preparing ultrathin MoS_2 nanosheets, the procedure presented here is simple, economical and safe. Thus, it could potentially be scaled up to produce large quantities of exfoliated MoS_2 nanosheets.

The obtained MoS_2–PAH nanosheets were first characterized by atomic force microscopy (AFM). The AFM image in Fig. S1a† and the line profile in the inset of Fig. S1a† reveal that they are very thin (below 2 nm), which is less than 3 layers. The scanning electron microscopy (SEM) image in Fig. S1b† indicates the size of MoS_2–PAH nanosheets is at the nanoscale. The morphology of the obtained MoS_2–PAH nanosheets was further characterized by high-resolution transmission electron microscopy (HRTEM). The corresponding fast Fourier transform (FFT) pattern (inset in Fig. S1c†) illustrates the hexagonal lattices of MoS_2, which is consistent with the typical hexagonal atomic structure of 2H-MoS_2.[24] Additionally, the magnified image (Fig. S1d†) of a representative monolayer MoS_2–PAH clearly shows the hexagonal lattices of the

obtained nanosheets with a lattice constant of 0.315 nm.[25] The crystalline structure of the as-prepared MoS₂–PAH nanosheets was further measured by powder X-ray diffraction (XRD). All the peaks shown in Fig. S1e† exhibit the characteristics of the hexagonal MoS₂ (JCPDS no. 03-065-7025) and no other impurities were found, revealing the high purity of the as-obtained product. The surface groups of the as-prepared MoS₂–PAH nanosheets were detected by Fourier transform infrared (FT-IR) spectroscopy. As shown in Fig. S1f,† the N–H stretch (around 3400 cm^{-1}), CH₂ vibrations (about 2900 cm^{-1}), N–H asymmetric bending (about 1610 cm^{-1}) and C–H bending (around 1510 cm^{-1}) confirm the successful modification of PAH molecules on MoS₂.

The composition and the chemical state of the as-prepared MoS₂–PAH nanosheets were confirmed by X-ray photoelectron spectroscopy (XPS). A typical XPS survey spectrum of the as-prepared MoS₂–PAH nanosheets shows the peaks attributed to O, N, C, Mo, Cl and S elements (Fig. S2a†). The calculated atomic ratio between Mo and S from XPS is about 1 : 2.4, which is close to the stoichiometric MoS₂. The high-resolution Mo 3d XPS spectra can be fitted well into two individual doublets (Fig. S2b†). The two peaks at 232.7 eV and 229.5 eV are attributed to the Mo 3d$_{3/2}$ and Mo 3d$_{5/2}$ binding energies for Mo^{4+}, respectively.[26,27] Meanwhile, the S 2p spectrum shows two peaks located at 163.5 eV and 162.3 eV (Fig. S2c†), which are characteristic of the S 2p$_{1/2}$ and S 2p$_{3/2}$ components of MoS₂, respectively.[26,27] The as-prepared MoS₂–PAH nanosheets exhibited good dispersibility in ultra-pure water. The zeta potential measurement of MoS₂–PAH nanosheets indicates they are highly positively charged when dispersed in ultrapure water below pH 8 (Fig. S2d†).

Hydrothermal synthesis for BNPs has significant economic and environmental advantages, and is the most common "bottom-up" method. To prepare the MoS₂–PtAg hybrid nanomaterials, H₂PtCl₆·6H₂O and AgNO₃ as metal precursors were reduced by HCHO under hydrothermal conditions and PtAg alloys were formed on the MoS₂–PAH nanosheets. The as-prepared MoS₂–PtAg nanohybrids were characterized in detail. Fig. 2a shows a typical TEM image of the as-prepared MoS₂–PtAg nanohybrids with a Pt/Ag feeding molar ratio of 3 : 1. One can see that PtAg NPs are regularly octahedral and well dispersed on the MoS₂–PAH nanosheets (Fig. S3a–e†). The average size of PtAg NPs is about 13 nm with narrow size distribution (Fig. S3f†). As one of the simplest Platonic solids, the octahedron is one end of the growth morphologies of Platonic solids with 8 equilateral triangle faces.[28] The HRTEM image in Fig. 2b shows the lattice fringes with an inter-fringe distance of 0.23 nm, which is between the distance of the face-centered cubic (fcc) Pt (0.226 nm, JCPDS no. 04-0802) and Ag (0.236 nm, JCPDS no. 04-0783) in the (111) plane. The result indicates the formation of a fcc PtAg nano-octahedron, which has high symmetry with the {111} lattice facet as the basal surface.[29–31] Owing to different radii, Ag and Pt atoms are compressed and stretched during the formation process of a fcc PtAg nano-octahedron, respectively, resulting in the corresponding change in the interatomic distance, thus the inter-
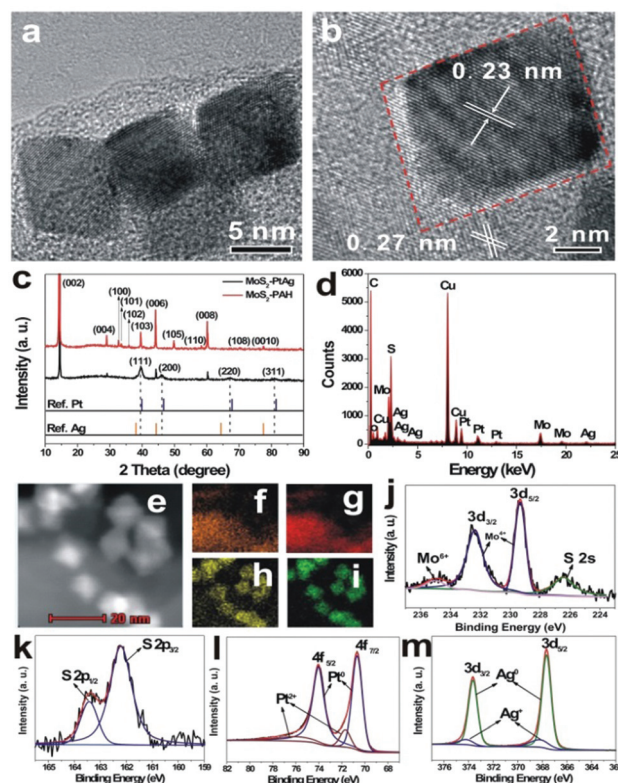

Fig. 2 Representative TEM image (a), HRTEM image (b), XRD pattern (c), EDX spectrum (d), high-angle annular dark-field scanning transmission electron microscope (HAADF-STEM) image (e), elemental maps for Mo (f), S (g), Pt (h) and Ag (i), peak-fitting XPS spectra of Mo 3d (j), S 2p (k), Pt 4f (l) and Ag 3d (m) regions of as-prepared MoS₂–PtAg hybrid nanomaterials. The Cu, C, O in TEM-based EDX pattern (d) originated from carbon film supported by copper grids.

fringe distance of PtAg is between Pt and Ag in the (111) plane. The lattice spacing of 0.27 nm belongs to the (100) plane of MoS₂[32] and is also observed in the same image. As shown in Fig. 2c, the crystalline structure of the MoS₂–PtAg nanohybrids was further examined by XRD. Diffraction peaks at 2θ values of 39.6°, 46.1°, 67.2° and 81.0° can be assigned to the (111), (200), (220) and (311) crystal planes of a PtAg fcc structure, respectively. The diffraction peaks positioned between the standard peaks of Pt (JCPDS no. 04-0802) and Ag (JCPDS no. 04-0783), demonstrating the formation of a bimetallic phase of Pt and Ag. The energy dispersive X-ray (EDX) analysis of MoS₂–PtAg shows that both the signals of Mo, S, Pt and Ag can be easily detected from these samples (Fig. 2d). The analysed atomic ratio (Pt/Ag) by inductively coupled plasma optical emission spectroscopy (ICP-OES) is 74 : 26, which is very close to the Pt/Ag feeding ratio of 3 : 1. According to the analysed ICP result, the loading amount of Pt₇₄Ag₂₆ NPs on MoS₂–PAH nanosheets is 29.0 wt%, which is slightly lower than the calculated value owing to the loss during the repeated washing and dissolving process. To further investigate the nanostructure of MoS₂–PtAg, the element distributions of Mo, S, Pt and Ag in the hybrid material were studied by using a high-angle

annular dark-field scanning transmission electron microscope (HAADF-STEM). From the representative STEM image (Fig. 2e) and its corresponding Mo, S, Pt and Ag elemental maps (Fig. 2f–i), it can be seen that both Pt and Ag are evenly distributed in each individual NP. The chemical state of the as-prepared MoS_2–PtAg was confirmed by XPS. The high-resolution Mo 3d XPS spectrum can be deconvoluted into four single peaks (Fig. 2j). The two peaks at 232.4 eV ($3d_{3/2}$) and 229.3 eV ($3d_{5/2}$) binding energies are attributed to Mo^{4+}, while the shoulder at 235.0 eV are likely assigned to Mo^{6+}.[27,33] Meanwhile, a peak at 226.2 eV corresponding to the S 2s line of MoS_2 can be found. Additionally, the S 2p spectrum shows two peaks located at 163.4 eV and 162.2 eV (Fig. 2k), which are characteristic of the S $2p_{1/2}$ and S $2p_{3/2}$ components of MoS_2, respectively.[26,27] The XPS spectrum of Pt 4f (Fig. 2l) displays two peaks at 74.0 eV ($4f_{5/2}$) and 70.7 eV ($4f_{7/2}$), which is indicative of elemental Pt^0.[34] From the fitting curves, the calculated percentage of Pt^0 species is about 83.4%. The Ag 3d spectrum of the sample (Fig. 2m) consists of two individual peaks at 373.6 eV ($3d_{3/2}$) and 367.6 eV ($3d_{5/2}$), which can be assigned to the Ag^0.[35] The calculated percentage of Ag^0 species is about 84.8% from the fitting curves. The above results indicate that the ultrathin MoS_2–PAH nanosheets are successfully decorated with octahedral $Pt_{74}Ag_{26}$ alloy NPs.

To understand the formation mechanism of MoS_2–PtAg nanohybrids, a series of control experiments were carried out. Under the standard reaction conditions, the use of Pt precursor alone gave spherical Pt NPs supported on the MoS_2 nanosheets (Fig. S4a†). However, replacing the Pt precursor with a Ag precursor failed to synthesize the corresponding MoS_2–Ag nanohybrids, suggesting that a Ag precursor alone cannot be reduced under the present conditions. Moreover, using different Pt/Ag feeding molar ratios, various nanohybrids of MoS_2–PAH nanosheet-supported octahedral PtAg NPs (Fig. S4b–4d†) can be obtained. Obviously, the introduction of Ag^+ species into the reaction system can favor the formation of octahedral PtAg NPs. It is noted that the use of a large amount of Ag precursors in excess of Pt precursors brings about a low yield of the final products, leading to a low loading of octahedral PtAg NPs on MoS_2 nanosheets (Fig. S4d†). It is known that the standard reduction potential (E) for Pt^{2+}/Pt (1.18 V) is more positive than that of the Ag^+/Ag (0.80 V) pair in the same coordination environment, Pt ions with high standard reduction potential could be reduced first. Meanwhile, the overlapped elemental maps of Pt and Ag (Fig. S5d†) reveal these two elements are uniformly distributed in each individual NP, suggesting the continuous addition of Pt and Ag atoms during the formation of a PtAg nano-octahedron. In addition, the EDX line scanning profile across a single Pt-Ag NP (Fig. S5e†) clearly shows Pt and Ag content change synchronously, verifying the structure of the alloy. The selected PtAg NP contains 74% of Pt and 26% of Ag, which is in good agreement with the ICP-OES result. Based on the above result and discussion, we speculate that the Pt nanocrystals as seeds were first formed on the MoS_2 nanosheets. With the quick diffusion of Ag^+ ions at high temperature, they were adsorbed strongly

on the Pt {100} facets, followed by the reduction by the pre-formed Pt seeds. As more and more Ag atoms continuously deposited on the Pt {100} facets,[36] active Ag atoms from the corners of the reaction intermediates were selectively removed by the oxidative etching process of dissolved oxygen in the reaction system.[37,38] With the periodic deposition of Pt and Ag atoms as well as the re-oxidation of the Ag atoms on the growing intermediates, an octahedral PtAg NP enclosed by {111} facets was formed.

2.2 Peroxidase-like activity of MoS_2–PtAg hybrid nanomaterials

To investigate the catalytic activity of the as-prepared hybrid nanomaterials, 3,3′,5,5′-tetramethylbenzidine (TMB), 2,2-azino-bis(3-ethylbenzothiazoline-6-sulfonic acid) (ABTS) and o-phenylenediamine (OPD) are chosen as chromogenic substrates to study the oxidase-like or peroxidase-like activities of MoS_2–$Pt_{74}Ag_{26}$. In the presence of H_2O_2, MoS_2–$Pt_{74}Ag_{26}$ nanohybrids can catalyze the oxidation of TMB, ABTS and OPD, producing the typical blue color for TMB, green color for ABTS and yellow color for OPD (Fig. 3), while the control experiments without MoS_2–$Pt_{74}Ag_{26}$ or without H_2O_2 showed negligible color variation (Fig. S6†). This result clearly indicates that MoS_2–$Pt_{74}Ag_{26}$ has a peroxidase-like activity.

To study the interaction between the as-prepared ultrathin MoS_2 nanosheets and PtAg NPs, several control experiments were performed. Compared to the MoS_2 nanosheets and unsupported $Pt_{73}Ag_{27}$ NPs (Fig. S7†), MoS_2–$Pt_{74}Ag_{26}$ hybrids display enhanced catalytic activity with the example of TMB oxidation (Fig. S8a†). Different from MoS_2 alone, MoS_2–$Pt_{74}Ag_{26}$ not only has larger surface area, but also provides abundant active sites for the adsorption of TMB molecules. Accordingly, lone-pair electrons can be readily transferred from the amino groups of TMB molecule to the hybrids, which gives rise to an increase in electron density and mobility in the
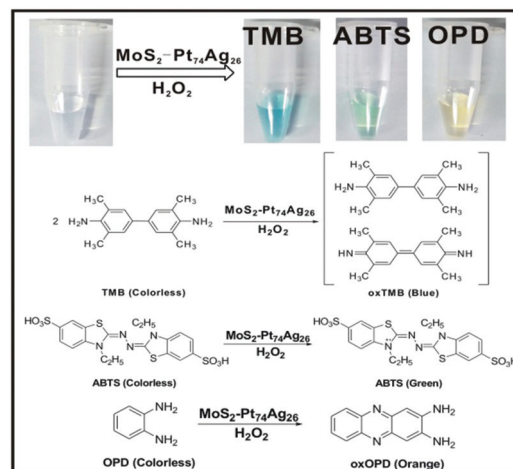

Fig. 3 The color change and corresponding reaction schemes for the oxidation of TMB, ABTS and OPD catalyzed by the as-prepared MoS_2–$Pt_{74}Ag_{26}$.

hybrids for electron transfer from hybrids to H_2O_2, leading to the reduction of H_2O_2 to H_2O and the reaction rate of TMB oxidation by H_2O_2 increases. The effect of Pt/Ag ratios of MoS_2–PtAg on their catalytic oxidation capability is also investigated. Fig. S8b† shows that MoS_2–$Pt_{74}Ag_{26}$ has the highest activity with the maximum absorbance at 652 nm. Thus, MoS_2–$Pt_{74}Ag_{26}$ is chosen as a typical enzyme mimetic for further studies. It has been found that MoS_2–$Pt_{74}Ag_{26}$ has good storage stability. When it has been stored in water at room temperature for 2 months, no obvious decrease in response to H_2O_2 is observed (Fig. S8c†). MoS_2–$Pt_{74}Ag_{26}$ also has good reusability after repeated cycles of H_2O_2 sensing as shown in Fig. S8d.† There is no apparent difference in morphology and size between the as-prepared hybrids and the recycled hybrids (Fig. S9†), indicating the stability of hybrids. The good stability and reusability of MoS_2–$Pt_{74}Ag_{26}$ makes it suitable and practical for a broad range of applications.

2.3 Reaction mechanism

Similar to HRP, the catalytic activities of MoS_2–PtAg show temperature, pH and H_2O_2 concentration dependence (Fig. S10†). MoS_2–$Pt_{74}Ag_{26}$ displays high catalytic activity at different pH values (3.0–6.0) and a wide range of temperatures (20–70 °C), while the catalytic activity of HRP was largely inhibited after incubation at pH below 4.0 or at temperature higher than 50 °C.[39] Thus, the robustness of MoS_2–$Pt_{74}Ag_{26}$ makes it potentially applicable under harsh conditions. For the catalytic oxidation of TMB by MoS_2–$Pt_{74}Ag_{26}$, the optimal pH is 4.0 and an optimal temperature is 50 °C. The peroxidase-like activity MoS_2–$Pt_{74}Ag_{26}$ is further investigated by the steady-state kinetic experiments. By monitoring the absorbance change at 652 nm for 30 min, typical Michaelis–Menten curves with TMB and H_2O_2 are obtained, respectively (Fig. 4a and b). Michaelis–Menten constant (K_m) and maximum initial rate (v_{max}) are obtained using the Lineweaver–Burk plot (Fig. 4c and d).
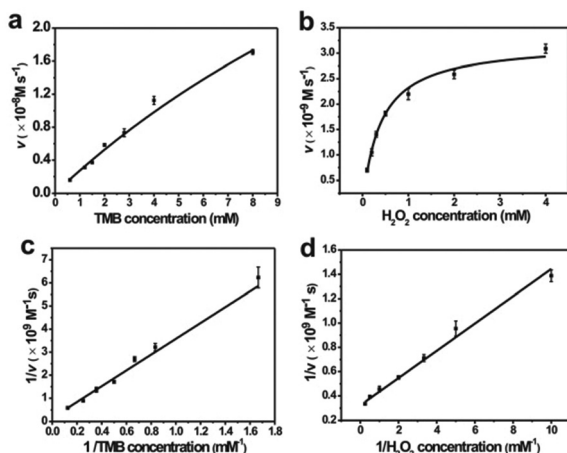
Table 1 Comparison of the apparent Michaelis–Menten constant (K_m) and maximum reaction rate (v_{max}) between MoS_2–$Pt_{74}Ag_{26}$ and HRP as well as MoS_2 nanosheets

Catalyst	Substrate	K_m [mM]	v_{max} [10^{-8} M s^{-1}]	Ref.
MoS_2–$Pt_{74}Ag_{26}$	TMB	25.71	7.29	This work
	H_2O_2	0.386	3.22	
HRP	TMB	0.434	10	40
	H_2O_2	3.7	8.71	
MoS_2 nanosheets	TMB	0.525	5.16	41
	H_2O_2	0.0116	4.29	

The apparent K_m value indicates the affinity of the substrates to enzymes and a lower value means a higher affinity. Table 1 lists the K_m and v_{max} values for MoS_2–$Pt_{74}Ag_{26}$, HRP and MoS_2 nanosheets. Compared to HRP, the K_m value for MoS_2–$Pt_{74}Ag_{26}$ with H_2O_2 as the substrate is lower, suggesting MoS_2–$Pt_{74}Ag_{26}$ has higher affinity for H_2O_2 than HRP. This can be understood since a HRP molecule contains only one iron ion which decomposes H_2O_2, while the surface of the mono-layer MoS_2 structure is decorated with lots of $Pt_{74}Ag_{26}$ NPs. The lower affinity for TMB can also guarantee more active sites would be available for H_2O_2. Meanwhile, the v_{max} value for MoS_2–$Pt_{74}Ag_{26}$ with TMB as the substrate was higher than MoS_2 alone. The synergistic effects of octahedral $Pt_{74}Ag_{26}$ NPs and ultrathin MoS_2 nanosheets as catalytic supports resulted in the improved catalytic activity of hybrids for colorimetric reactions.

The hydroxyl radical ($^{\bullet}OH$) as an important intermediate in peroxidase mimic-catalyzed colorimetric detection of H_2O_2 was studied extensively.[42,43] Here, the $^{\bullet}OH$ is assessed by adding terephthalic acid (TA) as a fluorescent probe into the H_2O_2/MoS_2–$Pt_{74}Ag_{26}$ system, where TA easily reacts with $^{\bullet}OH$ forming highly fluorescent 2-hydroxy terephthalic acid.[44] As shown in Fig. S11,† there is negligible fluorescence intensity in the absence of H_2O_2 or MoS_2–$Pt_{74}Ag_{26}$, while an emission peak at about 440 nm appears after MoS_2–$Pt_{74}Ag_{26}$ is added in the TA solution in the presence of H_2O_2, which indicates the production of $^{\bullet}OH$ after the interaction between MoS_2–$Pt_{74}Ag_{26}$ and H_2O_2. The result shows that MoS_2–$Pt_{74}Ag_{26}$ could decompose H_2O_2 to generate the $^{\bullet}OH$ radical. To further evaluate the effects of MoS_2–$Pt_{74}Ag_{26}$ on $^{\bullet}OH$ signal intensity, a series of electron spin resonance (ESR) experiments in the 5,5-dimethyl-1-pyrroline N-oxide (DMPO) spin trap system have been carried out. As shown in Fig. S12,† one can see that there are no apparent $^{\bullet}OH$ signals in the buffer/TMB/H_2O_2 system (curve a in Fig. S12†) while, the intensity of $^{\bullet}OH$ increases in the system of buffer/H_2O_2/MoS_2–$Pt_{74}Ag_{26}$ as time increases (curves b, c). However, after the addition of TMB to this solution, the signal of $^{\bullet}OH$ disappeared. Instead, a strong TMB cation radical[45] signal can be detected immediately (curve d in Fig. S12†). The above results indicate that MoS_2–$Pt_{74}Ag_{26}$ possesses peroxidase-like activity.

2.4 Detection of H_2O_2 and glucose

Based on the intrinsic peroxidase property of MoS_2–$Pt_{74}Ag_{26}$, the detection of H_2O_2 and glucose is designed using the blue

Fig. 4 Steady-state kinetic analysis using Michaelis–Menten model (a, b) and Lineweaver–Burk model (c, d) for MoS_2–$Pt_{74}Ag_{26}$. The concentration of H_2O_2 was 1 mM and TMB concentration was varied (a, c). The concentration of TMB was 1 mM and H_2O_2 concentration was varied (b, d).

color reaction catalyzed by MoS_2–$Pt_{74}Ag_{26}$. Fig. 5 shows the dependence of the absorbance at 652 nm on the concentration of H_2O_2, revealing that the intensity of absorption peak at 652 nm increases with increased H_2O_2 concentration from 1 μM to 1 mM. The upper and lower insets of Fig. 5 show the corresponding photographs of different solutions and the linear calibration plot, respectively. The estimated linear detection range and limit of detection (LOD) at a signal-to-noise ratio of 3 are listed in Table 2.

We also designed a method for the detection of glucose using the MoS_2–$Pt_{74}Ag_{26}$-based sensing system (see Experimental section). The dependence of the absorbance at 652 nm on the concentration of glucose from 1 μM to 1 mM is shown in Fig. 6a. One can see that the intensity of absorbance peak at 652 nm increases with increased glucose concentration. To examine the selectivity of the present assay toward glucose, detection experiments have been performed in the presence of glucose analogue substances including glucose, fructose, lactose and mannitol. A blue color solution was obtained in the presence of glucose, however, no obvious blue color is observed for other compounds although their concentration is 5-fold higher than that of glucose (Fig. 6b, inset). The above observations indicate that our sensing system exhibits excellent selectivity for glucose.
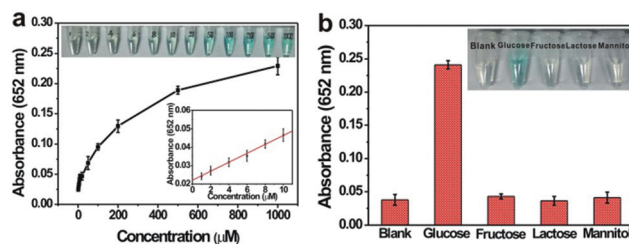

Fig. 6 (a) Dependence of the absorbance at 652 nm on the concentration of glucose from 1 μM to 1 mM. The upper and lower insets show the corresponding photographs of different solutions and linear calibration plot, respectively. (b) Selectivity analysis of MoS_2–$Pt_{74}Ag_{26}$/GOx/TMB system for glucose detection by measuring the absorbance at 652 nm (5 mM fructose, 5 mM lactose, 5 mM mannitol, and 1 mM glucose). Error bars represent the standard deviation for three measurements. Inset: photographs of different solutions.

The linear detection range and LOD for the detection of H_2O_2 and glucose are listed in Table 2. Lower LOD values are obtained with MoS_2–$Pt_{74}Ag_{26}$ as a peroxidase mimic, which indicates more sensitivity than the MoS_2 nanosheets.

3. Conclusions

In summary, novel MoS_2–$Pt_{74}Ag_{26}$ hybrid nanomaterials composed of octahedral $Pt_{74}Ag_{26}$ NP decorated ultrathin MoS_2 nanosheets have been successfully prepared by a facile and efficient method and investigated as peroxidase mimics. The obtained MoS_2–$Pt_{74}Ag_{26}$ hybrids have long-term stability and good reusability after repeated cycles of H_2O_2 sensing. MoS_2–$Pt_{74}Ag_{26}$ has higher affinity for H_2O_2 than HRP. Meanwhile, the v_{max} value for MoS_2–$Pt_{74}Ag_{26}$ with TMB was higher than MoS_2. The enhanced catalytic activity of hybrid nanomaterials for colorimetric reactions could be attributed to the synergistic effects of octahedral $Pt_{74}Ag_{26}$ NPs and ultrathin MoS_2 nanosheets as catalytic supports. With MoS_2–$Pt_{74}Ag_{26}$ nanohybrids, the production of active oxygen species ($^{\cdot}OH$) by H_2O_2 decomposition was responsible for the oxidation of TMB. On the basis of these findings, a colorimetric method with high sensitivity and selectivity for H_2O_2 and glucose detection has been developed. The detection of H_2O_2 and glucose are in a linear range from 1×10^{-6} to 5×10^{-5} mol L^{-1} and 1×10^{-6} to 1×10^{-5} mol L^{-1}, respectively, with the detection limit down to 4×10^{-7} mol L^{-1} for H_2O_2 and 8×10^{-7} mol L^{-1} for glucose. Lower LOD values have been obtained with MoS_2–$Pt_{74}Ag_{26}$ nanohybrids as peroxidase mimics, indicating that nanohybrids are more sensitive than MoS_2 nanosheets. Our approach can be potentially extended to the preparation of a series of other MoS_2–PtM nanohybrids (M = Pd, Rh, Au, Cu, Zn, Fe, Co, Ni, etc.) as peroxidase mimics. The present study provides a new avenue for developing highly sensitive sensors for biological and clinical diagnosis applications.

Fig. 5 Dependence of the absorbance at 652 nm on the concentration of H_2O_2 from 1 μM to 1 mM. The upper and lower insets show the corresponding photographs of different solutions and linear calibration plot, respectively.

Table 2 Comparison of linear range and LOD of this work with MoS_2 nanosheets as peroxidase mimics for colorimetric detection of H_2O_2 and glucose

| Peroxidase mimics | Linear range (μM) for | | LOD (μM) for | | |
	H_2O_2 detection	Glucose detection	H_2O_2 detection	Glucose detection	Ref.
MoS_2–$Pt_{74}Ag_{26}$	1–50	1–10	0.4	0.8	This work
MoS_2 nanosheets	5–100	5–150	1.5	1.2	41

4. Experimental section

4.1 Materials

Polyallylamine hydrochloride (molecular weight 120 000 to 200 000), silver nitrate, o-phenylenediamine (OPD), D-mannitol, L-cysteine and MoS_2 powder were supplied from Alfa Aesar. Chloroplatinic acid hexahydrate ($H_2PtCl_6 \cdot 6H_2O$) and 2,2′-azino-bis(3-ethylbenzo-thiazoline-6-sulfonic acid) diammonium salt (ABTS) were provided by J&K Scientific Ltd (Beijing, China). 3,3′,5,5′-Tetramethylbenzidine (TMB) was obtained from Acros. Terephthalic acid was bought from Sinopharm Chemical Reagent Co., Ltd (Shanghai, China). Formaldehyde solution (40%) was purchased from Xilong Chemical Co., Ltd (Shantou, China). H_2O_2 was provided by Beijing Chemical Works (Beijing, China). β-D-Glucose, α-lactose, D-fructose, and glucose oxidase (GOx, 50 KU, from *Aspergillus niger*) were purchased from Sigma-Aldrich. Other reagents and chemicals were at least analytical reagent grade. Ultrapure water was obtained by using a Milli-Q ultrapure system (18 MΩ cm).

4.2 Preparation of PAH-functionalized MoS_2 nanosheets

PAH-functionalized MoS_2 nanosheets (MoS_2–PAH) were prepared from commercial MoS_2 flakes *via* a simple liquid exfoliation method. Briefly, commercial MoS_2 powder (20 mg) was first ground with NaCl in a grinding miller for 2 h. Subsequently, the ground MoS_2 flakes were separated by dissolving NaCl with ultrapure water and then centrifuged. After being dried completely, the obtained MoS_2 flakes were dispersed in 20 mL of H_2SO_4 (95.0–98.0%) for intercalation at 90 °C overnight. Then the products were collected by centrifugation, repeatedly washed with ultrapure water to remove the residual H_2SO_4, and dispersed into 20 mL of ultrapure water. After that, 80 mg of PAH was added to the obtained dispersion under bath-sonication for 30 min. Then the solution was further probe-sonicated at a power of 325 W for 1 h and centrifuged at 2000 rpm for 10 min. Finally, the supernatant was collected and centrifuged at 12 000 rpm for 10 min to obtain MoS_2–PAH nanosheets.

4.3 Preparation of MoS_2–PtAg

Take the preparation of MoS_2–$Pt_{74}Ag_{26}$ hybrids for example. After 3 mL of MoS_2–PAH solution (about 0.1 mg mL^{-1}) was dispersed in 1 mL of ultrapure water, the solution was sonicated for 10 min, followed by addition of 0.3 μmol of $AgNO_3$, 0.9 μmol of H_2PtCl_6 and 10 μL of aqueous solution of HCHO solution (40%). Then the resulting mixture was transferred to 10 mL Teflon-lined stainless-steel autoclave and was heated at 180 °C for 4 h. After being cooled to room temperature, the obtained hybrid material was separated by centrifugation at 12 000 rpm for 10 min, washed with ultrapure water, and then dispersed into ultrapure water.

4.4 Characterization

Transmission electron microscopy (TEM) images were obtained using a FEI Tecnai G2 20 S-TWIN transmission electron microscope operating at an accelerating voltage of 200 kV.

Scanning electron microscopy (SEM) images were collected on a Hitachi S-4800 field-emission scanning electron microscope. X-ray powder diffraction (XRD) was performed using a Bruker D8 focus with Cu Kα radiation (λ = 1.5406 Å). High-resolution transmission electron microscopy (HRTEM) images were collected with a FEI Tecnai G2 F20 U-TWIN. Partial HRTEM images were collected on a JEOL JEM 2100F transmission electron microscope. Atomic force microscopy (AFM) characterization was performed on a Shimadzu SPM-9600 microscope. The composition of the products was measured by using a Thermo Scientific iCAP 6300 inductively coupled plasma optical emission spectrometer (ICP-OES). Zeta potential was measured using a Malvern Zetasizer Nano system. UV-Vis absorption spectroscopic measurements were carried out using a PerkinElmer Lambda 950 UV/VIS spectrophotometer. FT-IR spectra were recorded on a PerkinElmer Spectrum One FT-IR spectrometer in the transmission mode using CaF_2. X-ray photoelectron spectra (XPS) were recorded using a Thermo Fisher ESCALAB 250Xi X-ray photoelectron spectrometer. Binding energies (BE) were calibrated by setting the measured BE of C 1s to 284.8 eV. Electron spin resonance (ESR) spectra were recorded at room temperature on a JEOL JES-FA200 ESR spectrometer. DMPO (5,5-dimethyl-1-pyrroline N-oxide) was employed as the radical trap. Fluorometric measurements were carried out by using a Hitachi F-4600 fluorescence spectrophotometer.

4.5 Peroxidase-like activity of MoS_2–PtAg

In the presence of H_2O_2, the activity of MoS_2–$Pt_{74}Ag_{26}$ was investigated through the oxidation of TMB, ABTS and OPD to generate a colorimetric reaction. The reactions were carried out at room temperature using 18 nmol of MoS_2–$Pt_{74}Ag_{26}$ and 10 μL of H_2O_2 (33 mM) in 300 μL of NaAc buffer (pH 4.0) with 10 μL of substrate (50 mM).

4.6 Steady-state kinetic assays

The steady-state kinetic assays of the catalytic reactions were carried out at 50 °C in the TMB/H_2O_2/MoS_2–$Pt_{74}Ag_{26}$ reaction system. With TMB as the substrate, the kinetic analysis of MoS_2–$Pt_{74}Ag_{26}$ was performed with constant H_2O_2 concentration (1 mM) but varied TMB concentrations (0.6 to 8 mM). Meanwhile, with H_2O_2 as the substrate, the kinetic measurement was carried out with constant TMB concentration (1 mM) but varied H_2O_2 concentrations (0.1 to 4 mM).

Absorbance values monitored at 652 nm for all reactions were back-converted to TMB concentration derived oxidation products by the Beer–Lambert Law, $A = \varepsilon bC$; in which the molar absorption coefficient ε was 39 000 M^{-1} cm^{-1}, vitric cuvettes of path length b was 1 cm. Kinetic parameters were fitted based on the Michaelis–Menten equation:

$$v_0 = v_{max} \frac{[S]}{[S] + K_m}$$

where v_0 is the initial conversion rate, which can be calculated by the initial slope of absorbance changes with time, v_{max} is the maximum conversion rate, [S] is the substrate

concentration, and K_m is the Michaelis constant. The Line-weaver–Burk model $\frac{1}{v_0} = \frac{1}{v_{max}} + \frac{K_m}{v_{max}} \cdot \frac{1}{[S]}$ was also used to fit kinetic parameters.

4.7 Detection of H₂O₂ and glucose

For detection of H_2O_2, measurements were carried out by monitoring the absorbance change at 652 nm. In a typical run, 18 nmol of MoS_2–$Pt_{74}Ag_{26}$ was added into 300 μL of NaAc buffer solution (pH 4.0), followed by addition of 10 μL of TMB solution (50 mM in DMSO). After reaction for 30 min at 50 °C, the UV-vis spectra were recorded.

Glucose detection was performed according to the following three steps: (1) 100 μL of GOx (1 mg mL⁻¹) and 100 μL of glucose with different concentrations in 200 μL of Na_2HPO_4 buffer (10 mM, pH 7.0) were incubated at 37 °C for 1 h; (2) 10 μL of TMB (50 mM) and 18 nmol of MoS_2–$Pt_{74}Ag_{26}$ were added into the above solution; (3) the resulting mixture was incubated at 50 °C for 30 min before measurements.

Acknowledgements

Notes and references

1 K. S. Novoselov, A. K. Geim, S. V. Morozov, D. Jiang, Y. Zhang, S. V. Dubonos, I. V. Grigorieva and A. A. Firsov, *Science*, 2004, **306**, 666–669.

2 Q. H. Wang, K. Kalantar-Zadeh, A. Kis, J. N. Coleman and M. S. Strano, *Nat. Nanotechnol.*, 2012, **7**, 699–712.

3 M. Chhowalla, H. S. Shin, G. Eda, L. J. Li, K. P. Loh and H. Zhang, *Nat. Chem.*, 2013, **5**, 263–275.

4 X. Huang, Z. Zeng and H. Zhang, *Chem. Soc. Rev.*, 2013, **42**, 1934–1946.

5 J. Xie, J. Zhang, S. Li, F. Grote, X. Zhang, H. Zhang, R. Wang, Y. Lei, B. Pan and Y. Xie, *J. Am. Chem. Soc.*, 2013, **135**, 17881–17888.

6 G. Du, Z. Guo, S. Wang, R. Zeng, Z. Chen and H. Liu, *Chem. Commun.*, 2010, **46**, 1106–1108.

7 X. Huang, Z. Zeng and H. Zhang, *Chem. Soc. Rev.*, 2013, **42**, 1934–1946.

8 S. S. Singha, D. Nandi and A. Singha, *RSC Adv.*, 2015, **5**, 24188–24193.

9 A. J. Cheah, W. S. Chiu, P. S. Khiew, H. Nakajima, T. Saisopa, P. Songsiriritthigul, S. Radimane and M. A. A. Hamid, *Catal. Sci. Technol.*, 2015, **5**, 4133–4143.

10 L. Yuwen, F. Xu, B. Xue, Z. Luo, Q. Zhang, B. Bao, S. Su, L. Weng, W. Huang and L. Wang, *Nanoscale*, 2014, **6**, 5762–5769.

11 J. Deng, H. Li, J. Xiao, Y. Tu, D. Deng, H. Yang, H. Tian, J. Li, P. Ren and X. Bao, *Energy Environ. Sci.*, 2015, **8**, 1594–1601.

12 F. Cheng, J. Chen and X. Gou, *Adv. Mater.*, 2006, **18**, 2561–2564.

13 Z. Xiang, Z. Zhang, X. Xu, Q. Zhang, Q. Wang and C. Yuan, *Phys. Chem. Chem. Phys.*, 2015, **17**, 15822–15828.

14 X. Zhong, H. Yang, S. Guo, S. Li, G. Gou, Z. Niu, Z. Dong, Y. Lei, J. Jin, R. Li and J. Ma, *J. Mater. Chem.*, 2012, **22**, 13925–13927.

15 Z. Sun, Q. Zhao, G. Zhang, Y. Li, G. Zhang, F. Zhang and X. Fan, *RSC Adv.*, 2015, **5**, 10352–10357.

16 S. Su, C. Zhang, L. Yuwen, X. Liu, L. Wang, C. Fan and L. Wang, *Nanoscale*, 2016, **8**, 602–608.

17 C. Hou, Q. Xu, L. Yin and X. Hu, *Analyst*, 2012, **137**, 5803–5808.

18 K. Saha, S. S. Agasti, C. Kim, X. Li and V. M. Rotello, *Chem. Rev.*, 2012, **112**, 2739–2779.

19 K. S. Novoselov, D. Jiang, F. Schedin, T. J. Booth, V. V. Khotkevich, S. V. Morozov and A. K. Geim, *Proc. Natl. Acad. Sci. U. S. A.*, 2005, **102**, 10451–10453.

20 Y.-H. Lee, X.-Q. Zhang, W. Zhang, M.-T. Chang, C.-T. Lin, K.-D. Chang, Y.-C. Yu, J. T.-W. Wang, C.-S. Chang, L.-J. Li and T.-W. Lin, *Adv. Mater.*, 2012, **24**, 2320–2325.

21 H. S. S. R. Matte, A. Gomathi, A. K. Manna, D. J. Late, R. Datta, S. K. Pati and C. N. R. Rao, *Angew. Chem., Int. Ed.*, 2010, **49**, 4059–4062.

22 Z. Zeng, T. Sun, J. Zhu, X. Huang, Z. Yin, G. Lu, Z. Fan, Q. Yan, H. Hoon Hng and H. Zhang, *Angew. Chem., Int. Ed.*, 2012, **51**, 9052–9056.

23 J. N. Coleman, M. Lotya, A. O'Neill, S. D. Bergin, P. J. King, U. Khan, K. Young, A. Gaucher, S. De, R. J. Smith, I. V. Shvets, S. K. Arora, G. Stanton, H.-Y. Kim, K. Lee, G. T. Kim, G. S. Duesberg, T. Hallam, J. J. Boland, J. J. Wang, J. F. Donegan, J. C. Grunlan, G. Moriarty, A. Shmeliov, R. J. Nicholls, J. M. Perkins, E. M. Grieveson, K. Theuwissen, D. W. McComb, P. D. Nellist and V. Nicolosi, *Science*, 2011, **331**, 568–571.

24 F. Cheng, J. Chen and X. Gou, *Adv. Mater.*, 2006, **18**, 2561–2564.

25 J. P. Shi, M. Liu, J. Wen, X. Ren, X. Zhou, Q. Ji, D. Ma, Y. Zhang, C. Jin, H. Chen, S. Deng, N. Xu, Z. Liu and Y. Zhang, *Adv. Mater.*, 2015, **27**, 7086–7092.

26 Y. Shi, J.-K. Huang, L. Jin, Y.-T. Hsu, S. F. Yu, L.-J. Li and H. Y. Yang, *Sci. Rep.*, 2013, **3**, 1839.

27 L. Yang, W. Zhou, D. Hou, K. Zhou, G. Li, Z. Tang, L. Lia and S. Chen, *Nanoscale*, 2015, **7**, 5203–5208.

28 C. Li, K. L. Shuford, Q.-H. Park, W. Cai, Y. Li, E. J. Lee and S. O. Cho, *Angew. Chem., Int. Ed.*, 2007, **46**, 3264–3268.

29 Y. Wu, S. Cai, D. Wang, W. He and Y. Li, *J. Am. Chem. Soc.*, 2012, **134**, 8975–8981.

30 J. G. Zhang, Y. Gao, R. A. Alvarez-Puebla, J. M. Buriak and H. Fenniri, *Adv. Mater.*, 2006, **18**, 3233–3237.

31 C.-C. Chang, H.-L. Wu, C.-H. Kuo and M. H. Huang, *Chem. Mater.*, 2008, **20**, 7570–7574.

32 W. Zhou, Z. Yin, Y. Du, X. Huang, Z. Zeng, Z. Fan, H. Liu, J. Wang and H. Zhang, *Small*, 2013, **9**, 140–147.

33 Z. Chen, D. Cummins, B. N. Reinecke, E. Clark, M. K. Sunkara and T. F. Jaramillo, *Nano Lett.*, 2011, **11**, 4168–4175.

34 B. Zhou, Z. Sun, D. Li, T. Zhang, L. Deng and Y.-N. Liu, *Nanoscale*, 2013, **5**, 2669–2673.

35 L. Yuwen, F. Xu, B. Xue, Z. Luo, Q. Zhang, B. Bao, S. Su, L. Weng, W. Huang and L. Wang, *Nanoscale*, 2014, **6**, 5762–5769.

36 M. E. Grass, Y. Yue, S. E. Habas, R. M. Rioux, C. I. Teall, P. Yang and G. A. Somorjai, *J. Phys. Chem. C*, 2008, **112**, 4797–4804.

37 M. Liu, Y. Zheng, L. Zhang, L. Guo and Y. Xia, *J. Am. Chem. Soc.*, 2013, **135**, 11752–11755.

38 M. Jin, H. Zhang, Z. Xie and Y. Xia, *Energy Environ. Sci.*, 2012, **5**, 6352–6357.

39 J. Mu, Y. Wang, M. Zhao and L. Zhang, *Chem. Commun.*, 2012, **48**, 2540–2542.

40 L. Z. Gao, J. Zhuang, L. Nie, J. B. Zhang, Y. Zhang, N. Gu, T. H. Wang, J. Feng, D. L. Yang, S. Perrett and X. Y. Yan, *Nat. Nanotechnol.*, 2007, **2**, 577–283.

41 T. Lin, L. Zhong, L. Guo, F. Fu and G. Chen, *Nanoscale*, 2014, **6**, 11856–11862.

42 T. Zhang, Y. Lu and G. Luo, *ACS Appl. Mater. Interfaces*, 2014, **6**, 14433–14438.

43 L. Su, J. Feng, X. Zhou, C. Ren, H. Li and X. Chen, *Anal. Chem.*, 2012, **84**, 5753–5758.

44 K. Ishibashi, A. Fujishima, T. Watanabe and K. Hashimoto, *Electrochem. Commun.*, 2000, **2**, 207–210.

45 P. D. Josephy, T. Eling and R. P. Mason, *J. Biol. Chem.*, 1982, **257**, 3669–3675.